

GaussianHead: High-fidelity Head Avatars with Learnable Gaussian Derivation

Jie Wang, Jiu-Cheng Xie, Xianyan Li, Feng Xu, Chi-Man Pun, and Hao Gao

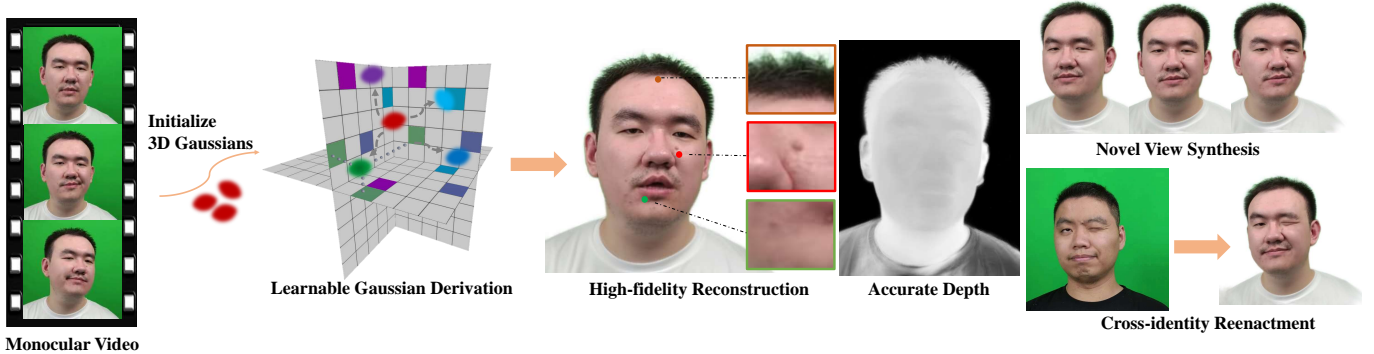


Fig. 1: Based on anisotropic 3D Gaussians and the learnable derivation strategies, our method learns an identity-specific head avatar from a monocular video of the corresponding subject. The proposed GaussianHead demonstrates outstanding performance in self-reconstruction, cross-identity reenactment, and novel-view synthesis tasks.

Abstract—Creating lifelike 3D head avatars and generating compelling animations for diverse subjects remain challenging in computer vision. This paper presents GaussianHead, which models the active head based on anisotropic 3D Gaussians. Our method integrates a motion deformation field and a single-resolution tri-plane to capture the head’s intricate dynamics and detailed texture. Notably, we introduce a customized derivation scheme for each 3D Gaussian, facilitating the generation of multiple “doppelgangers” through learnable parameters for precise position transformation. This approach enables efficient representation of diverse Gaussian attributes and ensures their precision. Additionally, we propose an inherited derivation strategy for newly added Gaussians to expedite training. Extensive experiments demonstrate GaussianHead’s efficacy, achieving high-fidelity visual results with a remarkably compact model size (≈ 12 MB). Our method outperforms state-of-the-art alternatives in tasks such as reconstruction, cross-identity reenactment, and novel view synthesis. The source code is available at: <https://github.com/chiehwangs/gaussian-head>.

Index Terms—Head avatar, 3D gaussian splatting, 3D reconstruction, hybrid neural network.

I. INTRODUCTION

CREATING personalized head avatars is very useful in wide-ranging applications like virtual reality, remote meetings, movies, and games. Previous works usually rely on synchronized multi-view images of heads to reconstruct

photorealistic 3D avatars [1]–[3]. The harsh capturing requirement hinders the wide range of popularity of these techniques among the public. An emergent exploration in this field focuses on using monocular videos to build personalized head avatars, which is much more convenient. Since almost all daily used smartphones now integrate high-quality cameras, this kind of technique has the potential to be used by all end users and may establish more applications like social communication and short video sharing. Nevertheless, the variable geometry and complex appearance of human heads make it very challenging to achieve precise modeling from single-view captures.

Early methods [4]–[6] in this direction are mostly based on pre-trained parametric models to create head avatars without details. Building implicit head avatars using Signed Distance Fields (SDF) [7], [8] helps overcome the deficiencies of parametric models and achieve better head geometry [9], [10]. Nevertheless, implicit surfaces lack enough expressive power for fine structures and suffer from inefficient rendering. To this end, combining structured data containers and volume rendering to build volumetric neural radiance fields gradually becomes the current mainstream practice. When it comes to the scope of head construction, [11], [12] utilize multi-resolution neural voxels as facial expression bases, combining them with expression parameters to produce visually compelling dynamic head avatars. Methods like [13], [14] leverage the tri-plane for feature storage, which produces impressive rendering effects and further reduces the quantity of model parameters [15], [16].

Despite the advantages of tri-plane-formed feature containers, their reliance on multi-resolution mechanism leaves room for further optimization of the model size. Moreover,

Jie Wang, Jiu-Cheng Xie, Xianyan Li and Hao Gao are with the School of Automation and the School of Artificial Intelligence, Nanjing University of Posts and Telecommunications, Nanjing, 210023, China. E-mail: chieh.wangs@gmail.com, jiuchengxie@gmail.com, 9745981xy@gmail.com, tsgaohao@gmail.com.

Feng Xu is with the School of Software and BNRist, Tsinghua University, Beijing 100084, China. E-mail: xufeng2003@gmail.com.

Chi-Man Pun is with the Department of Computer and Information Science, University of Macau, Taipa, Macau. E-mail: cmpun@um.edu.mo.

Jiu-Cheng Xie and Hao Gao are the corresponding authors.

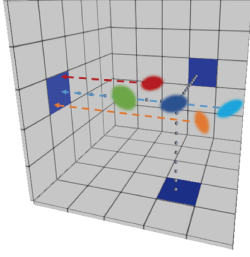


Fig. 2: The adoption of axis-aligned mapping is accompanied by a severe problem of “feature dilution”, detailed explanations of that are given in the third paragraph of the Introduction part.

the widely adopted axis-aligned mappings cause unexpected issues. Firstly, primitives on the same projection line (represented by the cyan, blue, and green blocks in Fig. 2) are repetitively mapped to the same position on the feature plane. Secondly, due to the finite resolution of the plane, primitives in close neighboring regions (the orange and red blocks in Fig. 2) may also be projected on the same grid. Consequently, the features stored at a particular grid point no longer exclusively or partially correspond to a specific primitive, which reduces the distinguishability among primitives, eventually weakening the representational capacity for sophisticated structures. This limitation is collectively referred to as “feature dilution” in this paper. Feature dilution becomes more pronounced in particular head areas with complex geometry, such as regions obscured by lips, hair, and wrinkles, where denser primitives often exist, accompanied by a significant occurrence of overlapping. TILTED [17] aims to achieve a more accurate feature representation of these primitives interpolated on the feature planes by rotating the entire scene simultaneously. While it appears to be effective in static scenarios, shortcomings arise in dynamic scenes. The inherent dynamism of objects disrupts those attempts to address biases in axis-aligned signals by relying on unified scene rotations. Additionally, since rotating the entire object does not change the relative topological structure, it is less effective in mitigating specific feature dilution within overlapped structures.

In this paper, we introduce the GaussianHead, a new method based on deformable 3D Gaussians for faithful head avatar construction and animation. It relies on shape-flexible 3D Gaussians and a compact tri-plane feature container, while a novel Gaussian derivation mechanism allows it to achieve high-quality rendering and competitive model size without relying on a multi-resolution paradigm. Notably, we disentangle the modeling of head geometry and texture attributes. To be concrete, a motion deformation field is first built to fit the whole head shape as well as the dynamic facial movements. In practice, it takes pre-retrieved facial expression coefficients as conditions to transform randomly initialized 3D Gaussians into a canonical space. Then we employ a compact data container—parameterized single-resolution tri-plane—to store the appearance information of those Gaussians. To resolve the aforementioned feature dilution problem, we design a novel Gaussian derivation strategy. In short, we generate multiple derivations of each core Gaussian in the canonical space using

the sets of learnable rotation transformations. By acquiring sub-features from these derived doppelgangers and integrating them, we are able to obtain the precise canonical features of the current Gaussians. Moreover, a mechanism of inheritance derivation initialization is adopted for newly added Gaussians in the later training phase, improving the convergence speed.

Contributions of this paper are summarized as follows:

- Leveraging anisotropic 3D Gaussian primitives and a parameterized tri-plane with a single resolution to represent the dynamic head avatar compactly.
- The novel strategy of deriving Gaussians effectively alleviates the feature dilution caused by axis-aligned mapping, resulting in a more accurate representation of the texture of complex facial structures.
- Extensive experiments have shown that our method is superior to the latest alternatives in terms of visual effects, quantitative metrics, and model sizes.

II. RELATED WORK

A. Scene Primitives in Reconstruction

Whether it is a real-world scenario, the human body, or a head, the foundation of their construction lies in a simple form of scene primitives. Some past approaches rely on implicit primitives. For instance, [7], [18], [19] use the signed distance function, which builds objects by tracing points located on the zero-level set of the function in space. [9], [20], [21] leverage the occupancy function to represent 3D surfaces as the continuous decision boundaries of deep neural network classifiers. However, these implicit primitives cannot represent complex head avatars. Methods based on neural radiance fields [22]–[27] store scenes using network weights. However, the necessary manner of constructing a large number of sample points in each ray always leads to significant training overhead. Explicit scene primitives, such as points [28]–[30], can capture sufficiently complex structures. However, due to the fixed shape of points, detailing can only be achieved by continuously refining point radii and increasing point counts during the training process, which introduces significant storage and training cost. Here, we use 3D anisotropic Gaussians [31] as scene primitives. They are deformable in geometric structure, allowing for the representation of intricate details by adjusting their shapes instead of blindly increasing quantity or reducing radii.

B. Sources for Head Portrait Synthesis

The widespread application of head avatars calls for convenient capture modes. Some studies [1]–[3], [32], [33] utilize dense multi-view or binocular vision to record dynamic head avatars in space. Among them, [32], [33] use 3D Gaussians combined with multi-view video to construct finely detailed head avatars. Although this brings better multi-view consistency, the difficulty of popularizing capture devices hinders the rapid adoption of such techniques. Meanwhile, [1], [2] reconstruct head dynamics along the temporal axis, sacrificing cross-subject generalization performance. Some portrait synthesis algorithms start with a single image or a set of

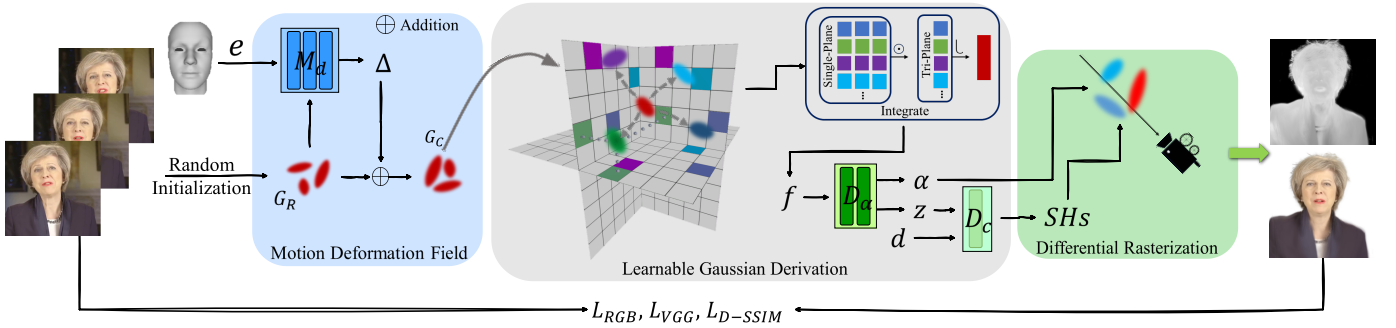


Fig. 3: *Method overview*. GaussianHead uses a set of 3D Gaussians with learnable attributes controlling their shape and appearance to model the subject’s head. A motion deformation field is first set up to represent the dynamic head geometry, which converts structureless Gaussians G_R to structured core ones G_C in a canonical space via conditioning on pre-acquired expression parameters e . Next, a single-resolution tri-plane structure of the feature container is leveraged to store appearance-related attributes. Notably, derivation mechanisms through learnable rotations are applied to each core Gaussian, yielding several doppelgangers of it. The integration of sub-features obtained through projection onto the planes from those doppelgangers is taken as the final canonical feature f of the core Gaussian. Two separate tiny MLPs are then employed to decode opacity α and spherical harmonic coefficients (SHs), based on which we generate the final rendering via differential rasterization. Notations \odot and \cup represent Hadamard product and concatenation operations, respectively.

images, constructing identity-consistent head avatars through image-to-image transformations. [34]–[37] leverage encoders to encode consistent identities from image sets and regulate outputs by fitting expressions or landmarks from the 3D morphable model. While achieving detailed rendered images, they lack multi-view consistency. Some head avatar methods decouple appearance [38] or track expressions and poses from monocular videos as reconstruction conditions [9], [11], [28], [39], [40], achieving increasingly realistic results. Similar to them, our approach also constructs the head avatars based on the monocular video of the target subject.

C. Hybrid Neural Field

Multiple implicit methods [9], [19], [20], [22] have found that, as the scene’s complexity increases, the learning difficulty for network models also increases. Recently, hybrid neural radiance fields have become popular, which use structured data containers (i.e., tri-plane [41], hexplane [15], [16], and voxel [42]) to store and a decoder to parse the information of scenes. In this manner, the encoding and decoding tasks are undertaken by multiple networks rather than one, reducing the modeling difficulty for each component. However, the commonly employed axis-aligned mappings by these methods will lead to imprecise representation of features. In addition, their multi-scale design has too many parameters, resulting in huge model sizes. We utilize the tri-plane structure and a decoder to represent a head based on Gaussian primitives in 3D space. The highlight of our approach is the proposed Gaussian derivation strategy and relevant adaptive designs to address the limitations of axis-aligned mapping through dispersing sub-features of each primitive, achieving excellent rendering performance with a small model size. We notice a concurrent work [43] also combines tri-plane with Gaussian splatting but is distinct from us in several aspects: they still query the feature of each Gaussian by projecting it to factored planes along three

axes, and they focus on synthesis in static scenarios while ours cares about the dynamic setting.

III. PRELIMINARY OF 3D GAUSSIAN SPLATTING

3D Gaussian Splatting [31] utilizes anisotropic 3D Gaussian primitives to explicitly represent the underlying structure of the scene. The structure of each Gaussian is determined by two parameters defined in world coordinates: position (mean) \mathbf{x} and 3D covariance matrix Σ ,

$$G(\mathbf{x}, \Sigma) = e^{-\frac{1}{2}\mathbf{x}^T \Sigma^{-1} \mathbf{x}}. \quad (1)$$

The intractable covariance matrix can be further decomposed into a scaling matrix \mathbf{S} and a rotation matrix \mathbf{R} , where the correlation between them is $\Sigma = \mathbf{R}\mathbf{S}\mathbf{S}^T\mathbf{R}^T$. For ease of optimization, we optimize a scaling vector \mathbf{s} for \mathbf{S} and a unit quaternion \mathbf{q} for \mathbf{R} in practice. Accordingly, the Gaussian is re-written as $G(\mathbf{x}, \mathbf{q}, \mathbf{s})$. In order to realize rendering, 3D Gaussians need to be projected onto the 2D image plane. Accordingly, the covariance matrix in camera coordinates can be obtained by $\Sigma' = \mathbf{J}\mathbf{W}\Sigma\mathbf{W}^T\mathbf{J}^T$, where \mathbf{W} denotes the view transformation matrix and \mathbf{J} represents the Jacobian matrix approximating the projective transformation [44], [45]. On the other hand, the appearance of every Gaussian is affected by the other two parameters, namely the opacity α and spherical harmonic coefficients Y_{lm} , which are combined with the spherical harmonic basis to represent view-dependent color. For each pixel on the image plane, its color is calculated by blending N ordered 3D Gaussians above it:

$$C = \sum_{i \in N} \mathbf{c}_i \alpha_i \prod_{j=1}^{i-1} (1 - \alpha_j), \quad (2)$$

where \mathbf{c}_i and α_i are the color and opacity of the i -th Gaussian individual overlapping the current pixel. During the training of those Gaussians, they undergo alternant densification according to the conditions of under- or over-reconstruction and

pruning primitives that do not contribute to the rendering results or have overlage sizes.

IV. APPROACH

Given a monocular video of the target person performing free head and facial movements, the corresponding expression parameters and masks of each frame, and known camera parameters, the proposed GaussianHead is trained on these four kinds of input. Our method models the complex head geometry based on anisotropic 3D Gaussians. A single-resolution tri-plane with a learnable derivation strategy is leveraged to encode texture information for those Gaussian primitives. Their integration ensures photorealistic rendering results. In inference, the approach allows high-fidelity reconstruction of the target subject and controllable animation by adjusting expression coefficients and view directions. Fig. 3 illustrates the overall workflow.

A. Motion Deformation Field

The original 3D Gaussian splatting technique was devised to reconstruct static scenes. However, human heads in our dynamic setting exhibit complex motions. Thus, we construct a motion deformation field to obtain variable Gaussians connected with the subject’s head motions, which are changeable within a period. Specifically, it first randomly initializes M Gaussians $G_R = \{G(\mathbf{x}_i, \mathbf{q}_i, \mathbf{s}_i)\}_{i=1}^M$, each of which is connected with three geometric attributes: position \mathbf{x} , rotation represented by unit quaternion \mathbf{q} , and scaling vector \mathbf{s} . Subsequently, the pre-acquired facial expression parameters \mathbf{e} and the positional encoding results of each Gaussian’s spatial coordinate \mathbf{x} are concatenated and then fed into a deformation network M_d with a multi-layer perceptron (MLP) as its implementation. For a certain Gaussian, the deformation network predicts $\Delta_{\mathbf{x}}$, $\Delta_{\mathbf{q}}$, and $\Delta_{\mathbf{s}}$, which are offsets in terms of position, rotation, and scale:

$$(\Delta_{\mathbf{x}}, \Delta_{\mathbf{q}}, \Delta_{\mathbf{s}}) = M_d(\gamma(\mathbf{x}), \mathbf{e}), \quad (3)$$

where γ represents conducting position encoding on the mean position of the current 3D Gaussian, generating a high-dimensional sine-cosine sequence [22]. Next, we add the obtained offsets to their initial states, yielding $\hat{\mathbf{x}}_i$, $\hat{\mathbf{q}}_i$, and $\hat{\mathbf{s}}_i$. Relevant updates are called core Gaussians $G_C = \{G(\hat{\mathbf{x}}_i, \hat{\mathbf{q}}_i, \hat{\mathbf{s}}_i)\}_{i=1}^M$ in the canonical space.

B. Learnable Gaussian Derivation

A single motion deformation MLP is sufficient to express complex head movements, but it struggles to simultaneously represent all fine and intricate facial textures (see Sec. V-G). To enhance the representation capability while using minor consumption, a *single-resolution tri-plane* is employed to encode texture information around the subject’s head. These factorized feature planes \mathbf{P}_{xy} , \mathbf{P}_{xz} , \mathbf{P}_{yz} have an identical size of (H, W, L) , where H and W represent the height and width and L denotes the channel length. Then, we derive K doppelgangers from each core Gaussian by imposing an equivalent number of learnable derivations parameterized by

unit quaternion \mathbf{r} on it. Note that K is required to evenly divide L . For every individual doppelganger, it is vertically projected onto three factor planes, generating three individual plane feature vectors by sequentially interpolating L/K channels of factor planes. Three shortened feature vectors from the tri-plane are fused by the Hadamard product, forming the sub-feature of the target doppelganger. Eventually, features from K doppelgangers are concatenated, yielding the canonical feature representation \mathbf{f} for the core Gaussian. Mathematically, that can be expressed as

$$\mathbf{f} = \bigcup_{k=1}^K \prod_{j=1}^3 \varphi(\mathbf{P}_j, \mathbf{r}_k(G_C)), \quad (4)$$

where \mathbf{P} represents the parameterized plane with j indexing the xy , xz , and yz factorized planes. The symbol \mathbf{r} denotes the derivation transformation, which is optimized also via a unit quaternion in our practice. In addition, φ indicates the projection of a doppelganger onto a factor plane and subsequent bilinear interpolation, and \bigcup means concatenating short features from multiple doppelgangers.

The unit quaternions controlling the derivation do not have an explicit first-order gradient. Due to manifold constraints, they cannot be straightforwardly optimized in Euclidean space using first-order optimizers. Therefore, we employ the Riemannian ADAM optimizer [46], where updates to unit quaternions at the training step t are induced by an exponential term based on the learning rate α_t and gradient ∇_t in their tangent space:

$$\mathbf{r}_{k,t+1} = \mathbf{r}_{k,t} \text{Exp}(\alpha_t \nabla_t). \quad (5)$$

C. Hierarchical Radiance Decoding and Inherited Derivation Initialization

In contrast to recent dynamic scene approaches based on 3D Gaussians [47], [48] that directly set opacity and color as optimizable parameters, we employ two small MLPs to decode the canonical features into opacity α and spherical harmonic coefficients Y_{lm} :

$$(\alpha, \mathbf{z}) = D_{\alpha}(\mathbf{f}), \quad (6)$$

$$Y_{lm} = D_c(\mathbf{d}, \mathbf{z}), \quad (7)$$

where \mathbf{z} denotes the intermediate latent code and \mathbf{d} is the view direction. We use 4th-order spherical harmonic coefficients to synthesize view-dependent colors. This design ensures a more precise inference of texture (validated in Sec. V-G). Finally, differentiable rasterization in Eq. 2 is used for rendering.

Recall that the number of Gaussian primitives dynamically increases or decreases during their training process. Given a new Gaussian copied by or split from the original entity, it proceeds to derive multiple doppelgangers via optimizable rotations in our method. Regarding the optimization of rotation parameters, we employ an inheritance initialization strategy, which means initializing them with the same values the parent Gaussian uses. Experiments show that, compared to random or zero initialization, the inheritance strategy increases the training speed by approximately 25%. We describe this setting in more detail and conduct experimental comparisons in Sec. V-F.

D. Training Objectives

We utilize L1 loss L_{RGB} to measure the pixel-wise difference between the ground truth image and its corresponding rendering. The perceptual loss L_{VGG} [49] and D-SSIM loss $L_{\text{D-SSIM}}$ are leveraged to measure the quality loss of the rendered images. Specifically, for the perceptual loss, we use the first four layers of the VGG model [50] to extract feature maps from compared image pairs for subsequent similarity computation. The full objective function as well as its components are given as follows:

$$L = \lambda_1 L_{\text{RGB}} + \lambda_2 L_{\text{VGG}} + \lambda_3 L_{\text{D-SSIM}}, \quad (8)$$

$$L_{\text{RGB}} = \|\mathbf{I} - \mathbf{I}^{\text{GT}}\|_1, \quad (9)$$

$$L_{\text{VGG}} = \|\text{VGG}(\mathbf{I}) - \text{VGG}(\mathbf{I}^{\text{GT}})\|_1, \quad (10)$$

$$L_{\text{D-SSIM}} = 1 - \text{SSIM}(\mathbf{I}, \mathbf{I}^{\text{GT}}), \quad (11)$$

where we empirically set $\lambda_1 = 0.8$, $\lambda_2 = 0.01$, and $\lambda_3 = 0.2$.

V. EXPERIMENTS

A. Datasets and Baselines

All monocular videos for experiments are sourced from public subjects, including real-life and internet recordings. We take the first part of every video clip for models' training, varying between 2000 and 2500 frames. The remaining ones constitute the testing samples. For each subject, we pre-process corresponding videos to get four modality signals: RGB head images with a unified resolution of 512×512 , expression parameters tracked by a 3DMM model [5], camera parameters, and binary masks predicted by MODNet [51]. Regarding the head movement, we follow the practice in [11], [23], which anchors the head in the coordinate system and simulates its pose changes with camera poses.

We compare our approach with four state-of-the-art methods for evaluation purposes. SplattingAvatar [40] binds 3D Gaussian to 3DMM, thus capable of utilizing the excellent rendering quality of 3D Gaussian and the effective motion control manner of 3DMM to construct a head avatar. INSTA [39] is based on volumetric NeRF and reconstructs avatars by building a neural surface on the foundation of 3DMM. PointAvatar [28] is based on explicit points and constructs detailed avatars through iterative refining and upsampling point clouds. NeRFBlendShape [11] constructs a hybrid NeRF and utilizes a multi-resolution hash grid to store facial expression bases.

B. Implementation Details

We implement GaussianHead with PyTorch, where differentiable 3D Gaussian rasterization is implemented based on CUDA kernels [31]. The initialization included 10K 3D Gaussians. Apart from optimizing the derivative quaternion using Riemannian ADAM [46], all other optimizers are first-order ADAM [52]. Specifically, for the unit quaternion \mathbf{q} representing 3D Gaussian rotation, we follow the explicitly first-order gradients as derived in [31] and also optimize it using ADAM. In our experiments, we set the batch size to

1 and train the model on a single RTX 3090, taking approximately 2 hours. After 3000 iterations, we perform densification and pruning on 3D Gaussians every 500 iterations, pruning Gaussians larger than a certain proportion of the scene and removing Gaussians with opacity below the threshold. We set the size threshold for large Gaussians to be greater than 1% of the scene and the opacity threshold to 0.0002. Other details follow the settings in [31].

For the tri-plane structural feature container, we set the size of each plane to $64 \times 64 \times 32$ ($H \times W \times L$). Regarding the derivative unit quaternions \mathbf{r} , they are treated as trainable parameters, initialized with random numbers in the range $[0, 2^{32}]$, and uniformly distributed on a 3-dimensional hypersphere to obtain unit quaternions with better distribution properties. Their learning rate decays from 1×10^{-3} to 0 at the last iteration.

C. Comparison with State-of-the-art Approaches

Reconstruction. This task is to construct a lifelike avatar of the target person in the reference video and make it perform the same actions. We showcase visual comparison results rendered by our method and baselines in Fig. 4. PointAvatar uses the built-in linear blend skinning (LBS) algorithm of 3DMM to control facial movements. By linearly combining expression coefficients and expression bases, this limited representation method often fails to accommodate extreme expressions. As evidence, please see the snap shots of avatars generated by this approach in Fig. 4, which fail to accurately depict mouth movements. Dynamic results in the supplementary video present a more intuitive demonstration of this particular deficiency. In addition, since the primitives adopted are points with fixed shapes, this approach may yield holes during reconstruction (7th row). SplattingAvatar binds Gaussians to the meshes of 3DMM, reducing redundant Gaussians in space. However, similar to PointAvatar, SplattingAvatar also relies on LBS to control facial expression movements. This results in inaccurate modeling of expressions, which is crucial to the head avatar. NeRFBlendShape occasionally produces artifacts (3rd row), which should be attributed to its adoption of a dynamic density grid update strategy, leading to inaccurate density estimation of sampling points around the head space. INSTA models the head based on a predefined 3DMM geometry, making it struggle to represent the fine structures (e.g., the jewelry in the 3rd and the suspended hair in the 6th row). In contrast, our GaussianHead can accurately render subtle details such as slightly closed eyes and wrinkles. Even if only a few frames show the oral cavity in the training data, we can achieve precise reconstruction (refer to Fig. 11). According to the best of our knowledge, this achievement is hard to obtain for previous head avatar approaches that also train their algorithms on monocular videos.

On the other hand, the error map, as opposed to the RGB image, can reflect the reconstruction accuracy more clearly. In practice, we calculate the L1 distance between the reconstructed images and the corresponding ground truth at the pixel level, the results of which are further mapped into the RGB space to produce the final error maps. Fig. 5



Fig. 4: Qualitative comparisons of the reconstruction task. All competitors are run under the configurations specified by their respective works. Our method achieves superior visual results, particularly in aspects such as wrinkles, teeth, eyebrows, and even reflections on glasses.

TABLE I: Quantitative comparisons of reconstruction quality. The six subjects in Fig. 4 are indexed as ID1-ID6 from top to bottom.

Method	ID1			ID2			ID3		
	PSNR \uparrow	SSIM \uparrow	LPIPS \downarrow	PSNR \uparrow	SSIM \uparrow	LPIPS \downarrow	PSNR \uparrow	SSIM \uparrow	LPIPS \downarrow
SplattingAvatar [40]	28.42	0.901	0.119	27.24	0.873	0.181	26.14	0.915	0.186
INSTA [39]	27.41	0.892	0.141	28.43	<u>0.906</u>	0.172	25.26	0.903	0.189
NeRFBlendShape [11]	29.32	0.911	0.102	29.45	0.904	0.133	<u>27.02</u>	0.959	0.083
PointAvatar [28]	26.76	0.861	0.162	23.78	0.803	0.191	24.61	0.794	0.182
GaussianHead (ours)	31.70	0.940	0.091	<u>29.21</u>	0.911	0.119	28.70	0.963	0.066
Method	ID4			ID5			ID6		
	PSNR \uparrow	SSIM \uparrow	LPIPS \downarrow	PSNR \uparrow	SSIM \uparrow	LPIPS \downarrow	PSNR \uparrow	SSIM \uparrow	LPIPS \downarrow
SplattingAvatar [40]	30.28	0.928	0.099	26.78	0.760	0.113	26.25	0.812	0.113
INSTA [39]	29.79	<u>0.931</u>	0.095	26.77	<u>0.791</u>	0.131	<u>27.19</u>	<u>0.876</u>	<u>0.095</u>
NeRFBlendShape [11]	29.98	0.905	<u>0.091</u>	<u>27.29</u>	0.789	<u>0.104</u>	26.22	0.832	0.128
PointAvatar [28]	27.11	0.898	0.142	23.36	0.642	0.154	24.71	0.717	0.185
GaussianHead (ours)	<u>30.06</u>	0.947	0.089	27.65	0.893	0.095	28.31	0.904	0.084

¹ The number with bold typeface means the best result and the underline is the second best.

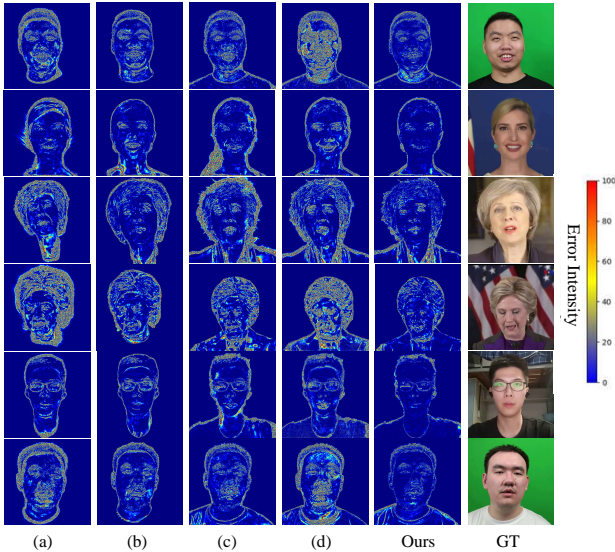


Fig. 5: Error maps for the reconstruction task. We compare with (a) SplattingAvatar [40], (b) INSTA [39], (c) NeRFBlendShape [11], and (d) PointAvatar [28]. In each map, brighter areas indicate larger errors. It is pointed out that the first two approaches do not support modeling of the torso part.

clearly shows that our method achieves better reconstruction accuracy than others. Evaluation results tabulated in Table I quantitatively demonstrate our superiority under three image quality related metrics.

Reenactment. This setting is more challenging than the reconstruction task because it aims to transfer the motion patterns of one real subject to the constructed avatar with a different identity. We showcase the reenactment results in Fig. 6. PointAvatar and SplattingAvatar struggle to reproduce even non-subtle and non-extreme expressions. In some frames, significant distortions in poses or expressions are observed. For illustration, in the first row of Fig. 6, PointAvatar fails to reproduce the neck’s state accurately. In the second row, SplattingAvatar cannot model the entire face successfully. The biggest problem with INSTA is the apparent loss of identity with the animated avatar. In other words, the digital embodiment in motion sequences does not resemble the corresponding

TABLE II: Quantitative comparisons of model size, training cost, and rendering time.

Method	Model Size (MB) \downarrow	Rendering Time (second) \downarrow	Train. Memory (GB) \downarrow	Infer. Memory (GB) \downarrow
SplattingAvatar [40]	84	0.04	11	5
INSTA [39]	60	0.06	16	3.5
NeRFBlendShape [11]	564	0.28	7.5	3
PointAvatar [28]	212	1.5	80	23
GaussianHead (ours)	12	0.09	<u>8.5</u>	2.5

¹ The number with bold typeface means the best and the underline is the second best.

² The average rendering time of a single frame is tested on a RTX3090.

subject in the monocular video it learns from. Note that this issue does not show up in the reconstruction results. NeRFBlendShape performs less satisfactorily in depicting facial details, as all the rendering frames appear over-smoothed. By comparison, the head avatars animated by GaussianHead excel at precisely reproducing the actions and poses of the source subject while depicting facial details and preserving identity consistency simultaneously. Our method still performs well even in imitating extreme facial expressions—for example, the first and third rows on the left side of Fig. 6.

More evaluations. Apart from rendering quality, we also conduct evaluations in multiple aspects and record the results in Table II. In brief, our method consumes the minimum GPU memory at inference time, smaller training resource and medium rendering speed with respect to other methods. It is especially noteworthy that we have a much smaller model size ($1/5$ of the second smallest) than competitors. It should be attributed to the derivation mechanism adopted in our framework, which allows the precise encoding of appearance information of 3D Gaussians with a single-resolution tri-plane-formed feature container. More detailed investigation of that will be given in Section V-G.

D. Novel View Synthesis and Depth Estimation

Avatars generated by the proposed GaussianHead exhibit remarkable multi-view consistency, as illustrated in Fig. 7. The results show no artifacts or unrealistic facial expressions. At the same time, our method can also accurately represent details, such as teeth, from novel perspectives. Based on the settings of previous work [48], we additionally present the reconstructed precise depth maps in Fig. 8, from which it can

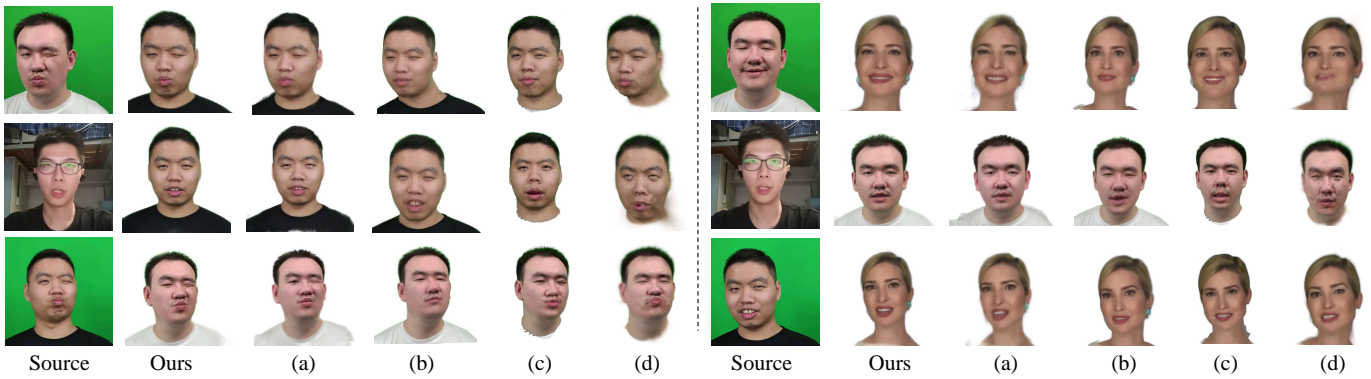


Fig. 6: Qualitative comparisons of the cross-identity reenactment task. Here, (a), (b), (c), and (d) respectively denote NeRFBlendShape [11], PointAvatar [28], INSTA [39], and SplattingAvatar [40]. Our GaussianHead achieves the best reenactment results, even in conveying extreme expressions. For more intuitive comparisons of motion sequences reenacted by these methods, please refer to the supplementary video.

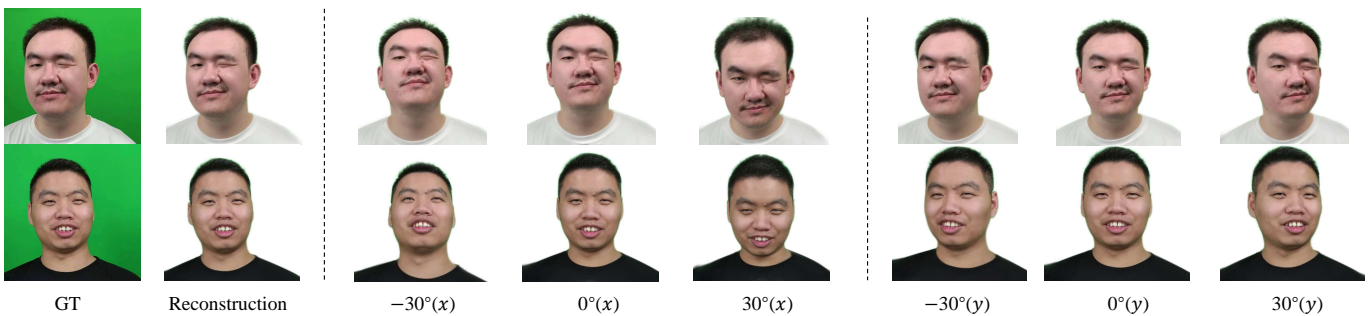


Fig. 7: Novel views rendered by our GaussianHead via rotating the camera viewpoint around the x or y axes. There exists a pronounced consistency in rendering details across these newly synthesized perspectives.

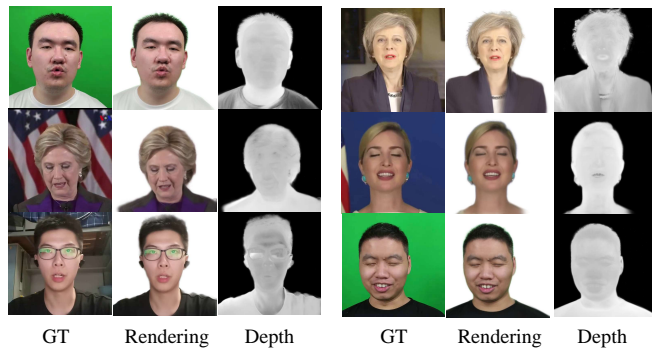


Fig. 8: We reconstruct the ground truth image (left) into a head avatar (center) and simultaneously visualized the depth estimated by GaussianHead (right). Our method obtains accurate depth information.

be clearly seen whether there is the presence of artifacts. Our method demonstrates excellent depth estimation performance.

E. Number of Doppelgangers

The number of derived doppelgangers (K) significantly influences training time and the final rendering results. We conduct experiments to determine the optimal value by setting

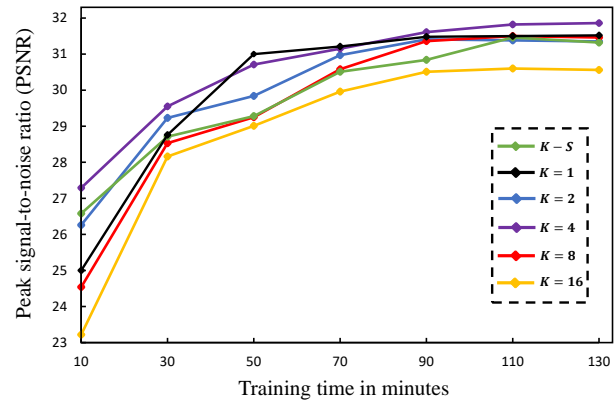


Fig. 9: The performance of taking different numbers of derived doppelgangers K during the training process (“ $K - S$ ” represents the K -scheduler). Optimal performance is achieved when setting K to 4.

it to five different values: 1, 2, 4, 8, and 16 (under the requirement that the count of channels L in each factor plane, set to 32 in our implementation, is divisible by K). Additionally, we also investigate an adaptive K -scheduler for a more comprehensive evaluation: increasing K with the

TABLE III: Performance of using different resolution mechanisms for tri-plane and different initialization strategies for Gaussian derivation.

Method	PSNR \uparrow	SSIM \uparrow	LPIPS \downarrow	Model Size (MB) \downarrow	Training Time (hours) \downarrow
M-res	29.89	0.931	0.090	136	~ 3
R-init	28.85	0.912	0.103	12	~ 2.5
Z-init	28.42	0.897	0.105	12	~ 2.5
Ours (S-res, I-init)	29.87	0.938	0.092	12	~ 2

growing number of Gaussians:

$$K = \frac{L}{2^{t-u}}, u = \left\lceil \frac{n_i}{n_o} \right\rceil, \quad (12)$$

where n_i and n_o are the current and initialized number of Gaussians, $\lceil \cdot \rceil$ denotes the ceiling function, and t is a constant set to 6. Relevant experimental results are shown in Fig. 9. In the context of a fixed value, an excessively large K results in optimization challenges, notably evidenced by a pronounced deceleration in the optimization process at $K = 8$ and 16. Conversely, fewer doppelgangers ($K = 1, 2$) are proven to be inadequate in addressing the issue of feature dilution, leading to a discernible deterioration in PSNR. On the other hand, the incorporation of an adaptive changing scheme (i.e., K -scheduler) does not yield superior outcomes, which should be partially attributed to the predominant occurrence of newly introduced Gaussians in vacant regions. These regions, in contrast to their densely optimized counterparts, have a lower likelihood of encountering feature dilution problems. According to the experimental results, we ultimately choose $K = 4$.

F. Initialization of Derivative Quaternion

In neural radiance fields [17], [22], the number of sampled points in the scene is mostly fixed. However, our Gaussian-Head undergoes densification or pruning of 3D Gaussians as the iterations progress. For the Gaussians that are clipped out, their quaternions used for controlling derivation are directly deleted. For the newly added ones that split from the parent Gaussian, three initialization schemes for derivative quaternions are studied: randomly initializing from the range $[0, 2^{32}]$ as done at the beginning of training (R-init), zero initialization (Z-init), and inheriting derivative parameters from the parent Gaussian (I-init). The time required for these three schemes to achieve their respective optimal rendering quality is reported in Table III. We observe that the inheriting initialization leads to better rendering results and quicker convergence than its two counterparts. We think these advantages stem from the relatively good starting values provided by the parent Gaussians, reducing the difficulty of parameters optimization.

G. Ablation Study

Unless otherwise stated, we conduct ablation experiments on the first three subjects and present the average results.

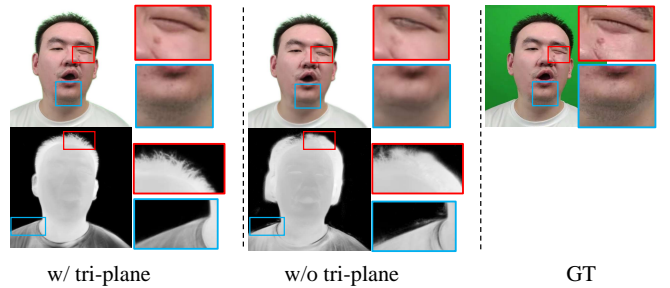


Fig. 10: Visual comparisons of with (w/) or without (w/o) employing the parametric tri-plane structure to store Gaussian appearance information.

TABLE IV: Ablation studies on several key components of our GaussianHead.

Method	L1 \downarrow	PSNR \uparrow	SSIM \uparrow	LPIPS \downarrow
w/o tri-plane	0.0014	28.53	0.891	0.144
w/o derivation	0.0013	28.89	0.912	0.115
w/o Δ_s	-	-	-	-
w/o Δ_q	0.0015	28.25	0.901	0.099
w/o Δ_s and Δ_q	-	-	-	-
w/o perceptual loss	0.0017	27.82	0.897	0.151
Direct deform	0.0035	24.55	0.792	0.319
Global rotation	0.0015	28.31	0.901	0.110
Decoded by MLP	0.0023	26.42	0.871	0.195
Ours full	0.0010	29.87	0.938	0.092

¹ The leading dash (-) means the model dose not converge.

² The number with bold typeface means the best and the underline is the second best.

Parametric tri-plane. Our method employs a parametric tri-plane as the container to store Gaussian appearance information. For comparison, we ablate the parametric tri-plane and directly set the opacity and spherical harmonic coefficients connected with 3D Gaussians as optimizable parameters (“w/o tri-plane”). The ablation results given in Fig. 10 validate the effectiveness of our design. The depth maps yielded by directly optimizing these two radiance parameters lead to numerous redundant Gaussians around the head that will not be removed because their opacity value is above the pre-defined threshold. This inevitably increases training overhead and causes negative perceptual impacts (pay attention to the enlarged local area on the face).

Furthermore, to demonstrate the advantages of parameterized tri-plane in compactly and accurately encoding texture-related knowledge, we replace it with a multi-layer perceptron (“Decoded by MLP”) having a comparable number of parameters. Regarding this variant, our pipeline consists of two MLPs, one for the motion deformation field and the other for decoding texture semantic information from canonical Gaussians. When checking its results in Fig. 11, we find that in region not commonly seen in the training videos, such as the oral cavity, it usually renders facial components in colors different from the ground truth. In contrast, our GaussianHead with tri-plane gives precise texture reproduction, even like the lip color and the highlight above earrings. Quantitative results summarized in Table IV align with this observation.

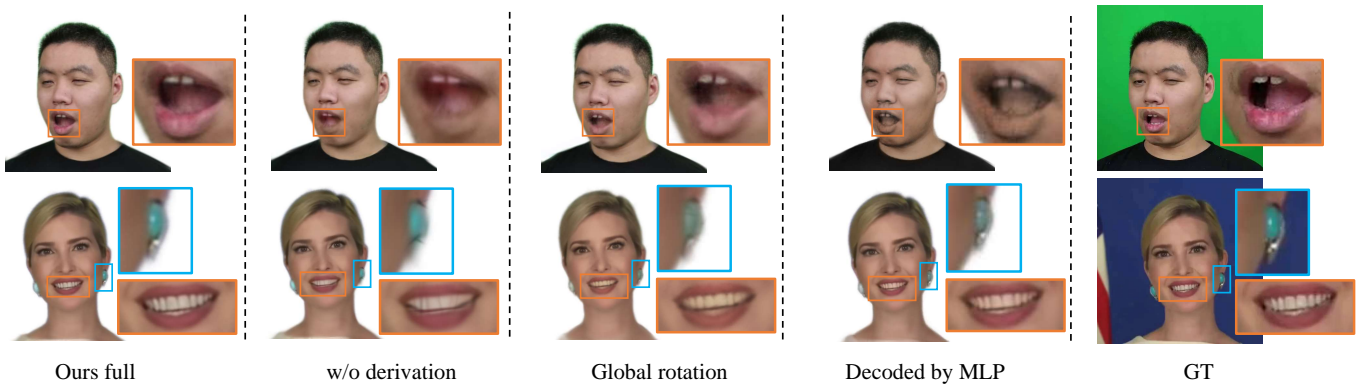


Fig. 11: Qualitative demonstration of partial ablation experiments. The novel Gaussian derivation strategy accurately restores features representing various complex structure regions, enabling the high-fidelity rendering of subtle details even for oral cavity rarely seen in the training data.

Learnable Gaussian derivation. We make ablation experiments using axis-aligned mappings, following the practice in the traditional tri-plane [15], [41] (“w/o derivation”). Compared to our GaussianHead leveraging the derivation strategy, this variant performs worse in expressing high frequency signals. Additionally, we imitate TILTED [17] by adopting a fixed set of rotations for the entire scene (“Global rotation”) rather than individual primitives. The experimental results support our analysis in Sec. I, global rotation is unsuitable for complex dynamic scenarios.

Multi-resolution tri-plane. In works like k-planes [15] and hexplane [16], the multi-resolution mechanism of tri-plane is crucial for obtaining high-quality results because of the feature extraction at different scales. However, it also leads to an increase of model size. We investigate the impacts of using this design in our framework (following the settings of previous work [15], we use multiple resolutions of [64, 128, 256, 512] in this experiment). Relevant results in Table III show that the induced improvement in rendering quality is almost negligible, whereas the model size grows dramatically. Meanwhile, utilizing a single-resolution tri-plane in our method already achieves comparable visual effects. This should be attributed to the proposed Gaussian derivation strategy, which allows the efficient and precise representation of facial appearance.

Motion deformation field. The motion deformation field is crucial to express dynamic-related expressions. It deserves further exploration on whether directly learning the deformed geometric attributes or predicting their offsets relative to current values. We start with our investigation by separately removing Δ_q (“w/o Δ_q ”), Δ_s (“w/o Δ_s ”) and both of them (“w/o Δ_q and Δ_s ”) to evaluate their influence. This means that during final rendering, we directly take the initialized rotation q , scaling s or both of them as the geometric attributes of deformed 3D Gaussians in the canonical space. Experiments show that after removing Δ_s , some Gaussians begin to fluctuate uncontrollably, either becoming too large or too small, leading to the failure of model convergence.

We push forward the ablation by using a MLP to directly predict the properties of 3D Gaussians in the canonical space. In this setup, the deformation field predicts all geometric

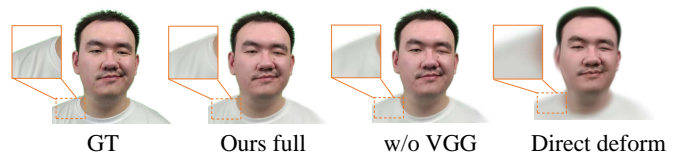


Fig. 12: Visual results without employing perceptual loss and using direct deformation field.

parameters of canonical 3D Gaussians, rather than estimating relevant residual values and then adding them to the initials. We report relevant performance (“Direct deform”) in Table IV and Figure 12. The experimental results indicate that, both in terms of quantitative metrics and visual effects, predicting the geometric properties of canonical Gaussians directly rather than their residual values yields significantly inferior results. We deduce that direct inference poses many difficulties to the network in specifically distinguishing head regions influenced by dynamic expression parameters, resulting in widespread blurring in areas outside the face.

Perceptual loss. During the training process, our GaussianHead is supervised by minimizing a perceptual loss, actually striving to shorten the distance between the features extracted from two images using a pre-trained VGG [50] model. We observe that employing this loss effectively preserves the consistency in details between the rendered image and its origin reference. By comparison, the removal of it causes a significant decrease in the rendering quality, as evidenced by the results in Fig. 12 and Table IV.

VI. DISCUSSION

Although our method achieves excellent visual effects, it does not separate the motion of the head and torso. Instead, it still uses camera parameters as rough proxies for pose parameters, which is a common practice in some avatar works (e.g., NeRFBlendShape [11] and INSTA [39]). However, this may result in unnatural shoulder shaking in scenarios with significant motion differences between the head and torso (see Fig. 13). Existing separation methods either utilize semantic masks for independent training of these two parts [13], [53],



Fig. 13: Failure case. When significant movement occurs in the ground truth (left), the rendered avatar’s torso (middle) will exhibit visible corresponding movement. For clarity, we extract and superimpose their contours (right) for comparison. Compared to the ground truth contours (green), the contours of the rendered avatar (blue) show certain offsets in the torso. Please refer to the supplementary video for the animation.

[54] or explicitly control their motions separately using the LBS algorithm of 3DMM [9], [28]. The former complicates the entire training process, making it unable to achieve end-to-end training and incurring additional training overhead. The latter, while capable of separately controlling the broad-range pose movements of the head and torso, performs poorly in controlling subtle expressions (because it is difficult for 3DMM to represent most complex expressions), as demonstrated by the expression distortion issues in the supplementary video of PointAvatar. Therefore, exploring a practical end-to-end method that achieves separate control of partial structures on the head while effectively expressing subtle facial expressions should be a valuable direction for future work. Some promising solutions include:

- Endowing each Gaussian with a new attribute to reveal which part it models—the head or the torso. Being aware of this, we can construct a deformation field purely responsible for facial dynamics and use the LBS to control the articulated changes in head and torso poses.
- Incorporating a virtual joint approach similar to the one used in [55] to compensate for muscle movements not fully controlled by LBS, thereby addressing the limitations of 3DMM in expression control.

VII. CONCLUSION

In conclusion, this paper introduces GaussianHead, a novel approach leveraging 3D anisotropic Gaussians to construct high-fidelity head avatars and produce reliable animations. Our method presents an effective framework for utilizing Gaussian primitives to model geometrically variable heads with continuous motions and represent complex textures. With its compact single-resolution tri-plane feature structure and innovative derivation strategy, GaussianHead demonstrates exceptional performance in handling challenging scenarios, such as intricate skin details, voluminous hair, limited training data for oral cavities, and extreme facial expressions, all while maintaining a considerably small model size. We anticipate that GaussianHead will serve as a valuable source of inspiration for the followers.

ACKNOWLEDGMENTS

This work was supported in part by National Nature Science Foundation of China under Grant 62301278, Grant 62371254,

Grant 61931012; in part by Nature Science Foundation of Jiangsu Province of China under Grant BK20230362 and Grant BK20210594; and in part by Natural Science Research Start-up Foundation of Recruiting Talents of Nanjing University of Posts and Telecommunications under Grant NY222019 and Grant NY221019.

REFERENCES

- [1] T. Kirschstein, S. Qian, S. Giebenhain, T. Walter, and M. Nießner, “Nersemble: Multi-view radiance field reconstruction of human heads,” *arXiv preprint arXiv:2305.03027*, 2023.
- [2] K. Teotia, X. Pan, H. Kim, P. Garrido, M. Elgharib, C. Theobalt *et al.*, “Hq3davator: High quality controllable 3d head avatar,” *arXiv preprint arXiv:2303.14471*, 2023.
- [3] C. Cao, V. Agrawal, F. De La Torre, L. Chen, J. Saragih, T. Simon, and Y. Sheikh, “Real-time 3d neural facial animation from binocular video,” *ACM Transactions on Graphics*, vol. 40, no. 4, pp. 1–17, 2021.
- [4] V. Blanz and T. Vetter, “A morphable model for the synthesis of 3d faces,” in *Seminal Graphics Papers: Pushing the Boundaries, Volume 2*, 2023, pp. 157–164.
- [5] T. Gerig, A. Morel-Forster, C. Blumer, B. Egger, M. Luthi, S. Schönborn, and T. Vetter, “Morphable face models—an open framework,” in *Proceedings of the IEEE International Conference on Automatic Face and Gesture Recognition*, 2018, pp. 75–82.
- [6] T. Li, T. Bolkart, M. J. Black, H. Li, and J. Romero, “Learning a model of facial shape and expression from 4d scans,” *ACM Transactions on Graphics*, vol. 36, no. 6, pp. 194–1, 2017.
- [7] L. Yariv, Y. Kasten, D. Moran, M. Galun, M. Atzmon, B. Ronen, and Y. Lipman, “Multiview neural surface reconstruction by disentangling geometry and appearance,” in *Proceedings of the Advances in Neural Information Processing Systems*, 2020, pp. 2492–2502.
- [8] L. Yariv, J. Gu, Y. Kasten, and Y. Lipman, “Volume rendering of neural implicit surfaces,” in *Proceedings of the Advances in Neural Information Processing Systems*, 2021, pp. 4805–4815.
- [9] Y. Zheng, V. F. Abrevaya, M. C. Bühler, X. Chen, M. J. Black, and O. Hilliges, “Im avatar: Implicit morphable head avatars from videos,” in *Proceedings of the IEEE/CVF Conference on Computer Vision and Pattern Recognition*, 2022, pp. 13 545–13 555.
- [10] C. Lin, K. Nagano, J. Kautz, E. Chan, U. Iqbal, L. Guibas, G. Wetzstein, and S. Khamis, “Single-shot implicit morphable faces with consistent texture parameterization,” in *ACM SIGGRAPH 2023 Conference Proceedings*, 2023, pp. 1–12.
- [11] X. Gao, C. Zhong, J. Xiang, Y. Hong, Y. Guo, and J. Zhang, “Reconstructing personalized semantic facial nerf models from monocular video,” *ACM Transactions on Graphics*, vol. 41, no. 6, pp. 1–12, 2022.
- [12] Y. Xu, L. Wang, X. Zhao, H. Zhang, and Y. Liu, “Avatarmav: Fast 3d head avatar reconstruction using motion-aware neural voxels,” in *Proceedings of the ACM SIGGRAPH*, 2023, pp. 1–10.
- [13] J. Li, J. Zhang, X. Bai, J. Zhou, and L. Gu, “Efficient region-aware neural radiance fields for high-fidelity talking portrait synthesis,” in *Proceedings of the IEEE/CVF International Conference on Computer Vision*, 2023, pp. 7568–7578.
- [14] Z. Peng, W. Hu, Y. Shi, X. Zhu, X. Zhang, H. Zhao, J. He, H. Liu, and Z. Fan, “SyncTalk: The devil is in the synchronization for talking head synthesis,” *arXiv preprint arXiv:2311.17590*, 2023.
- [15] S. Fridovich-Keil, G. Meanti, F. R. Warburg, B. Recht, and A. Kanazawa, “K-planes: Explicit radiance fields in space, time, and appearance,” in *Proceedings of the IEEE/CVF Conference on Computer Vision and Pattern Recognition*, 2023, pp. 12 479–12 488.
- [16] A. Cao and J. Johnson, “Hexplane: A fast representation for dynamic scenes,” in *Proceedings of the IEEE/CVF Conference on Computer Vision and Pattern Recognition*, 2023, pp. 130–141.
- [17] B. Yi, W. Zeng, S. Buchanan, and Y. Ma, “Canonical factors for hybrid neural fields,” in *Proceedings of the IEEE/CVF International Conference on Computer Vision*, 2023, pp. 3414–3426.
- [18] L. Yariv, P. Hedman, C. Reiser, D. Verbin, P. P. Srinivasan, R. Szeliski, J. T. Barron, and B. Mildenhall, “BakedSDF: Meshing neural SDFs for real-time view synthesis,” *arXiv preprint arXiv:2302.14859*, 2023.
- [19] J. J. Park, P. Florence, J. Straub, R. Newcombe, and S. Lovegrove, “DeepSDF: Learning continuous signed distance functions for shape representation,” in *Proceedings of the IEEE/CVF Conference on Computer Vision and Pattern Recognition*, 2019, pp. 165–174.

- [20] L. Mescheder, M. Oechsle, M. Niemeyer, S. Nowozin, and A. Geiger, "Occupancy networks: Learning 3d reconstruction in function space," in *Proceedings of the IEEE/CVF Conference on Computer Vision and Pattern Recognition*, 2019, pp. 4460–4470.
- [21] S. Peng, M. Niemeyer, L. Mescheder, M. Pollefeys, and A. Geiger, "Convolutional occupancy networks," in *Proceedings of the European Conference on Computer Vision*, 2020, pp. 523–540.
- [22] B. Mildenhall, P. P. Srinivasan, M. Tancik, J. T. Barron, R. Ramamoorthi, and R. Ng, "Nerf: Representing scenes as neural radiance fields for view synthesis," *Communications of the ACM*, vol. 65, no. 1, pp. 99–106, 2021.
- [23] G. Gafni, J. Thies, M. Zollhofer, and M. Nießner, "Dynamic neural radiance fields for monocular 4d facial avatar reconstruction," in *Proceedings of the IEEE/CVF Conference on Computer Vision and Pattern Recognition*, 2021, pp. 8649–8658.
- [24] R. Martin-Brualla, N. Radwan, M. S. Sajjadi, J. T. Barron, A. Dosovitskiy, and D. Duckworth, "Nerf in the wild: Neural radiance fields for unconstrained photo collections," in *Proceedings of the IEEE/CVF Conference on Computer Vision and Pattern Recognition*, 2021, pp. 7210–7219.
- [25] H. Zhang, F. Li, J. Zhao, C. Tan, D. Shen, Y. Liu, and T. Yu, "Controllable free viewpoint video reconstruction based on neural radiance fields and motion graphs," *IEEE Transactions on Visualization and Computer Graphics*, vol. 29, no. 12, pp. 4891–4905, 2022.
- [26] K. Wang, S. Peng, X. Zhou, J. Yang, and G. Zhang, "Nerfcap: Human performance capture with dynamic neural radiance fields," *IEEE Transactions on Visualization and Computer Graphics*, vol. 29, no. 12, pp. 5097–5110, 2022.
- [27] L. Song, A. Chen, Z. Li, Z. Chen, L. Chen, J. Yuan, Y. Xu, and A. Geiger, "Nerfplayer: A streamable dynamic scene representation with decomposed neural radiance fields," *IEEE Transactions on Visualization and Computer Graphics*, vol. 29, no. 5, pp. 2732–2742, 2023.
- [28] Y. Zheng, W. Yifan, G. Wetzstein, M. J. Black, and O. Hilliges, "Pointavatar: Deformable point-based head avatars from videos," in *Proceedings of the IEEE/CVF Conference on Computer Vision and Pattern Recognition*, 2023, pp. 21 057–21 067.
- [29] Q. Xu, Z. Xu, J. Philip, S. Bi, Z. Shu, K. Sunkavalli, and U. Neumann, "Point-nerf: Point-based neural radiance fields," in *Proceedings of the IEEE/CVF Conference on Computer Vision and Pattern Recognition*, 2022, pp. 5438–5448.
- [30] A. Mao, Z. Du, J. Hou, Y. Duan, Y.-j. Liu, and Y. He, "Pu-flow: A point cloud upsampling network with normalizing flows," *IEEE Transactions on Visualization and Computer Graphics*, vol. 29, no. 12, pp. 4964–4977, 2022.
- [31] B. Kerbl, G. Kopanas, T. Leimkühler, and G. Drettakis, "3d gaussian splatting for real-time radiance field rendering," *ACM Transactions on Graphics*, vol. 42, no. 4, pp. 1–14, 2023.
- [32] Y. Xu, B. Chen, Z. Li, H. Zhang, L. Wang, Z. Zheng, and Y. Liu, "Gaussian head avatar: Ultra high-fidelity head avatar via dynamic gaussians," *arXiv preprint arXiv:2312.03029*, 2023.
- [33] S. Qian, T. Kirschstein, L. Schoneveld, D. Davoli, S. Giebenhain, and M. Nießner, "Gaussianavatars: Photorealistic head avatars with rigged 3d gaussians," *arXiv preprint arXiv:2312.02069*, 2023.
- [34] Z. Zhang, Y. Ge, R. Chen, Y. Tai, Y. Yan, J. Yang, C. Wang, J. Li, and F. Huang, "Learning to aggregate and personalize 3d face from in-the-wild photo collection," in *Proceedings of the IEEE/CVF Conference on Computer Vision and Pattern Recognition*, 2021, pp. 14 214–14 224.
- [35] W. Yu, Y. Fan, Y. Zhang, X. Wang, F. Yin, Y. Bai, Y.-P. Cao, Y. Shan, Y. Wu, Z. Sun *et al.*, "'nofa: Nerf-based one-shot facial avatar reconstruction,'" in *Proceedings of the ACM SIGGRAPH*, 2023, pp. 1–12.
- [36] Z. Zhang, R. Chen, W. Cao, Y. Tai, and C. Wang, "Learning neural proto-face field for disentangled 3d face modeling in the wild," in *Proceedings of the IEEE/CVF Conference on Computer Vision and Pattern Recognition*, 2023, pp. 382–393.
- [37] S. Liu and J. Hao, "Generating talking face with controllable eye movements by disentangled blinking feature," *IEEE Transactions on Visualization and Computer Graphics*, vol. 29, no. 12, pp. 5050–5061, 2022.
- [38] Y. Hong, B. Peng, H. Xiao, L. Liu, and J. Zhang, "Headnerf: A real-time nerf-based parametric head model," in *Proceedings of the IEEE/CVF Conference on Computer Vision and Pattern Recognition*, 2022, pp. 20 374–20 384.
- [39] W. Zielonka, T. Bolkart, and J. Thies, "Instant volumetric head avatars," in *Proceedings of the IEEE/CVF Conference on Computer Vision and Pattern Recognition*, 2023, pp. 4574–4584.
- [40] Z. Shao, Z. Wang, Z. Li, D. Wang, X. Lin, Y. Zhang, M. Fan, and Z. Wang, "SplattingAvatar: Realistic Real-Time Human Avatars with Mesh-Embedded Gaussian Splatting," in *Proceedings of the IEEE/CVF Computer Vision and Pattern Recognition*, 2024.
- [41] E. R. Chan, C. Z. Lin, M. A. Chan, K. Nagano, B. Pan, S. De Mello, O. Gallo, L. J. Guibas, J. Tremblay, S. Khamis *et al.*, "Efficient geometry-aware 3d generative adversarial networks," in *Proceedings of the IEEE/CVF Conference on Computer Vision and Pattern Recognition*, 2022, pp. 16 123–16 133.
- [42] T. Müller, A. Evans, C. Schied, and A. Keller, "Instant neural graphics primitives with a multiresolution hash encoding," *ACM Transactions on Graphics*, vol. 41, no. 4, pp. 1–15, 2022.
- [43] Z.-X. Zou, Z. Yu, Y.-C. Guo, Y. Li, D. Liang, Y.-P. Cao, and S.-H. Zhang, "Triplane meets gaussian splatting: Fast and generalizable single-view 3d reconstruction with transformers," *arXiv preprint arXiv:2312.09147*, 2023.
- [44] M. Zwicker, H. Pfister, J. Van Baar, and M. Gross, "Ewa splatting," *IEEE Transactions on Visualization and Computer Graphics*, vol. 8, no. 3, pp. 223–238, 2002.
- [45] V. B. J. Zwicker Matthias, Pfister Hanspeter and G. Markus, "Surface splatting," in *Proceedings of the Annual Conference on Computer Graphics and Interactive Techniques*, 2001, pp. 371–378.
- [46] G. Bécigneul and O.-E. Ganea, "Riemannian adaptive optimization methods," *arXiv:1810.00760*, 2018.
- [47] G. Wu, T. Yi, J. Fang, L. Xie, X. Zhang, W. Wei, W. Liu, Q. Tian, and X. Wang, "4d gaussian splatting for real-time dynamic scene rendering," *arXiv preprint arXiv:2310.08528*, 2023.
- [48] Z. Yang, X. Gao, W. Zhou, S. Jiao, Y. Zhang, and X. Jin, "Deformable 3d gaussians for high-fidelity monocular dynamic scene reconstruction," *arXiv preprint arXiv:2309.13101*, 2023.
- [49] R. Zhang, P. Isola, A. A. Efros, E. Shechtman, and O. Wang, "The unreasonable effectiveness of deep features as a perceptual metric," in *Proceedings of the IEEE/CVF Conference on Computer Vision and Pattern Recognition*, 2018, pp. 586–595.
- [50] K. Simonyan and A. Zisserman, "Very deep convolutional networks for large-scale image recognition," *arXiv:1409.1556*, 2014.
- [51] Z. Ke, J. Sun, K. Li, Q. Yan, and R. W. Lau, "Modnet: Real-time trimap-free portrait matting via objective decomposition," in *Proceedings of the AAAI Conference on Artificial Intelligence*, vol. 36, no. 1, 2022, pp. 1140–1147.
- [52] D. P. Kingma and J. Ba, "Adam: A method for stochastic optimization," *arXiv preprint arXiv:1412.6980*, 2014.
- [53] Y. Guo, K. Chen, S. Liang, Y. Liu, H. Bao, and J. Zhang, "Ad-nerf: Audio driven neural radiance fields for talking head synthesis," in *Proceedings of the IEEE/CVF International Conference on Computer Vision*, 2021.
- [54] J. Tang, K. Wang, H. Zhou, X. Chen, D. He, T. Hu, J. Liu, G. Zeng, and J. Wang, "Real-time neural radiance talking portrait synthesis via audio-spatial decomposition," *arXiv preprint arXiv:2211.12368*, 2022.
- [55] J. Lei, Y. Wang, G. Pavlakos, L. Liu, and K. Daniilidis, "Gart: Gaussian articulated template models," *arXiv preprint arXiv:2311.16099*, 2023.